



# Explaining Spectral Line Profiles in the Horsehead Nebula Using Cloud Surface Curvature

Student  
Ducheng Lu

Supervisors  
Franck Le Petit (LERMA)  
Emeric Bron (LERMA)

Jan 2025

## Abstract

The interstellar medium (ISM), composed of gas and dust between stars in galaxies, plays a critical role in star formation and galactic evolution. Interactions between the ISM and massive stars or star clusters shape its physical and chemical properties. One key region where these processes take place is the photodissociation region (PDR), where far-ultraviolet radiation dominates the chemical and heating processes. PDRs are the primary sources of infrared line and continuum radiation in galaxies, which are essential for probing PDR properties. PDR models have been instrumental in interpreting observational data; however, they have limitations, such as the use of one-dimensional slab geometry. This project develops a wrapper for the MeudonPDR code to compute column densities in spherical geometry and convolve them with instrument resolution, offering a more accurate model of line emission. Additionally, preliminary work on solving radiative transfer along the line of sight in spherical geometry is presented. These modifications improve the alignment between model and observed spatial profiles of emission lines along a cut in the Horsehead Nebula, both in shape and extent. The solution for radiative transfer in spherical geometry is still under development, and further improvements in profile modeling are anticipated. This work will enhance the interpretation of observational data and the determination of physical parameters from PDR models.

## Abstract

Le milieu interstellaire (MIS), composé de gaz et de poussières entre les étoiles des galaxies, joue un rôle essentiel dans la formation des étoiles et l'évolution des galaxies. Les interactions entre le MIS et les étoiles massives ou les amas d'étoiles façonnent ses propriétés physiques et chimiques. Une région clé où ces processus ont lieu est la région de photodissociation (PDR), où le rayonnement ultraviolet lointain domine les processus chimiques et de chauffage. Les régions de photodissociation sont les principales sources de raies et de rayonnement continu dans le domaine infrarouge des galaxies, ce qui est essentiel pour sonder les propriétés des régions de photodissociation. Les modèles PDR ont joué un rôle important dans l'interprétation des données d'observation; cependant, ils ont des limites, comme l'utilisation d'une géométrie unidimensionnelle. Ce projet développe un wrapper pour le code MeudonPDR afin de calculer les densités de colonne en géométrie sphérique et de les convoluer avec la résolution de l'instrument, offrant un modèle plus précis des profils spatiaux d'émission des raies. En outre, des travaux préliminaires sur la résolution du transfert radiatif le long de la ligne de visée en géométrie sphérique sont présentés. Ces modifications améliorent l'alignement entre le modèle et les profils spatiaux de raies le long d'une coupe dans la nébuleuse de la Tête de Cheval, à la fois en termes de forme et d'étendue. La solution pour le transfert radiatif en géométrie sphérique est encore en cours de développement, et d'autres améliorations dans la modélisation des profils sont attendues. Ce travail améliorera l'interprétation des données d'observation et la détermination des paramètres physiques à partir des modèles PDR.

## Contents

<b>1</b>	<b>Introduction</b>	<b>1</b>
1.1	Photodissociation Regions (PDRs) . . . . .	1
1.2	The Horsehead Nebula . . . . .	2
1.3	Motivation . . . . .	3
<b>2</b>	<b>Data</b>	<b>3</b>
<b>3</b>	<b>Methods</b>	<b>4</b>
3.1	The MeudonPDR code . . . . .	4
3.1.1	Constant Pressure vs. Constant Density . . . . .	6
3.1.2	Models with Exact Radiative Transfer of H <sub>2</sub> . . . . .	6
3.1.3	Models with Surface Chemistry . . . . .	7
3.2	Modeling Column Densities in a Spherical PDR . . . . .	9
3.3	Solving the Radiative Transfer Equation . . . . .	10
3.4	Convolution of Line Profiles with Instrumental Resolution	12
<b>4</b>	<b>Results and Discussion</b>	<b>12</b>
4.1	Convolved Column Densities from Spherical Model . . . . .	12
4.2	Effect of Cloud Radius on Column Densities . . . . .	13
4.3	Line Profiles with Radiative Transfer . . . . .	14
<b>5</b>	<b>Conclusions</b>	<b>15</b>
	<b>Supplementary Material</b>	<b>18</b>

# 1 Introduction

The interstellar medium (ISM), composed of gas and dust between stars in galaxies, plays a critical role in star formation and galactic evolution, constituting approximately 10% of the total baryonic mass (Draine 2011). The ISM is a dynamic environment where radiation, cosmic rays, magnetic fields, and turbulence interact with gas and dust, shaping its physical and chemical properties. It is the main site of star formation and serves as a matter reservoir for this process. In turn, massive stars and star clusters can disturb nearby molecular clouds through their strong stellar winds, ultraviolet (UV) radiation, and, at times, transient events like supernovae. This influence extends across various regions, from the diffuse edges of molecular clouds to their cold, dense cores. One such key region where these processes take place is the photodissociation region (PDR), which forms at the interface between molecular clouds and sources of UV radiation.

## 1.1 Photodissociation Regions (PDRs)

Photodissociation regions (PDRs) are regions of neutral gas where far-ultraviolet (FUV;  $6 \text{ eV} < h\nu < 13.6 \text{ eV}$ ) radiation dominates the chemical and heating processes (Tielens and Hollenbach 1985). A PDR begins at the ionization front (IF), where photons with energies above the Lyman limit (13.6 eV) are fully absorbed, preventing further ionization of hydrogen. PDRs span a wide range of incident FUV fluxes and densities, including all neutral gas in the ISM and molecular layers where FUV radiation drives molecule formation.

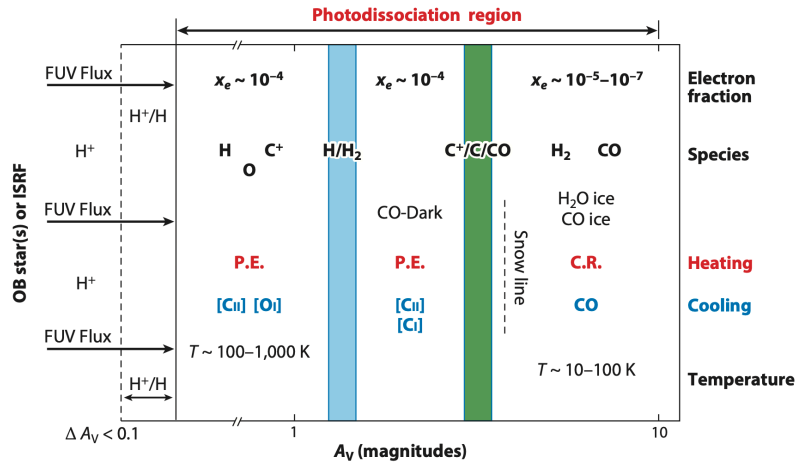


Figure 1: Schematic of a photodissociation region as a function of visual extinction  $A_V$ . Reprinted from Wolfire et al. (2022), Fig. 2. Red text indicates the dominant heating mechanisms, with "P.E." referring to photoelectric effects and "C.R." referring to cosmic rays. Blue text represents the main line emissions, which are the main cooling mechanisms.

PDRs are the primary sources of infrared (IR) line and continuum radiation in galaxies (Crawford et al. 1985; Stacey et al. 2010). Grains absorb the majority of the FUV radiation and re-radiate it in the IR continuum, but a fraction of the FUV photons heat the gas through, which then cool through line emission. Together, the line and continuum emission provide important insights into the physical and chemical conditions in PDRs. The study of PDRs is vital for understanding star formation and galaxy evolution. Observations of PDRs help to constrain key physical parameters such as temperature, chemical

composition, and radiative energy, probing the local environments of star-forming regions and the potential presence of stellar feedback.

Fig. 1 shows a one-dimensional (1D) structure of PDR illuminated by radiation field from the left. The adjacent  $\text{H}_{\text{II}}$  region absorbs extreme-ultraviolet (EUV;  $h\nu > 13.6 \text{ eV}$ ) photons, leaving FUV photons that create the PDR. Atomic hydrogen, helium, and oxygen are neutral because their ionization potentials exceed  $13.6 \text{ eV}$ , while molecules are photodissociated, and metals like carbon, silicon, and sulfur are singly ionized. The heating process is dominated by photoelectric effect on small grains and polycyclic aromatic hydrocarbons (PAHs), and the cooling process is dominated by fine-structure line emission. As the depth increases and FUV radiation diminishes,  $\text{H}_2$  forms, followed by CO. Both  $\text{H}_2$  and CO photodissociate via line absorption and can therefore self-shield, allowing them to form closer to the surface than other molecules like  $\text{H}_2\text{O}$  and its isotopologues, which dissociate via FUV continuum. In the deepest layers, cosmic rays dominate the heating process, and rotational transitions of CO isotopologues become the primary coolants.

## 1.2 The Horsehead Nebula

The Horsehead Nebula (Fig. 2 and cover image) is a well-known PDR that has been extensively studied in the literature. It is illuminated by  $\sigma$  Orionis, a O9.5V binary star system (Warren and Hesser 1977), located  $3.5 \text{ pc}$  from the edge of the PDR (Abergel et al. 2003; Schirmer et al. 2020), resulting in an incident FUV radiation field of around  $2.7 \times 10^{-3} \text{ erg s}^{-1} \text{ cm}^{-2}$  (Habart et al. 2005).

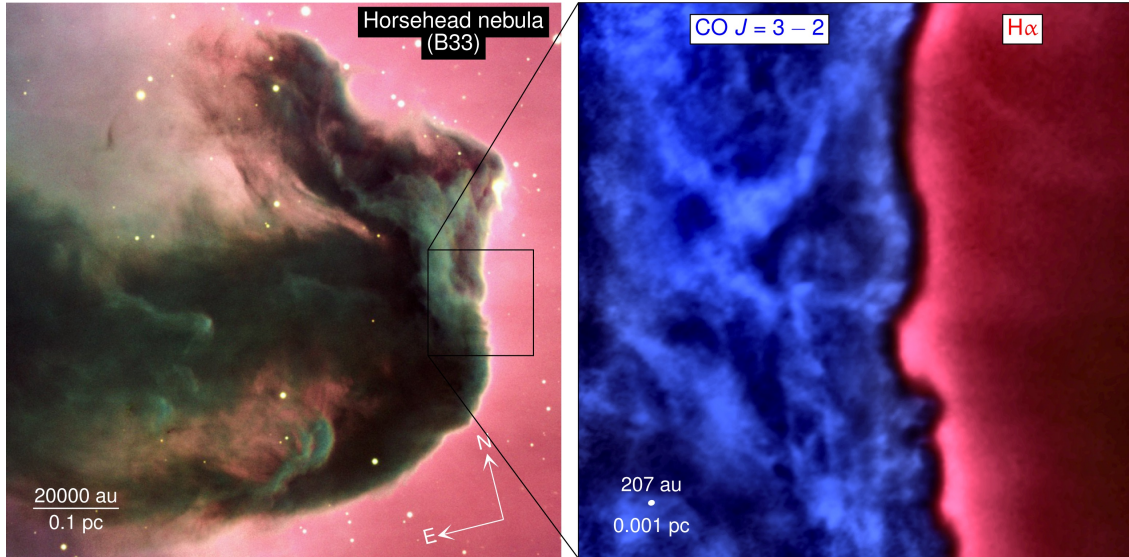


Figure 2: Multiphase view of the Horsehead nebula (Barnard 33). Reprinted from Hernández-Vera et al. (2023). Left: Composite color image of the Horsehead nebula observed with the VLT (ESO). Right: Zoomed-in view of the edge of the molecular cloud, imaged with ALMA in the CO  $J = 3 - 2$  line emission (blue) and the 0.9 m KPNO telescope in the  $\text{H}\alpha$  line emission. The dark region represents the neutral atomic layer.

In observational studies, it is customary to use arcseconds as the distance unit. As the Horsehead PDR is located approximately  $400 \text{ pc}$  from us (Menten et al. 2007; Schlafly et al. 2014), the distance unit can be converted as:

$$\alpha["] = \frac{d[\text{pc}]}{400 \text{ pc}} \frac{1''}{1 \text{ rad}}. \quad (1)$$



This gives  $1''$  corresponding to 1.9 mpc. The horsehead PDR is nearly edge-on, with an upper limit for the angle of  $6^\circ$  (Habart et al. 2005).

### 1.3 Motivation

While 1D PDR models have been instrumental in advancing our understanding of PDRs, they come with some limitations. Classic PDR models assume a 1D slab, plane-parallel geometry, which treats the cloud as infinite and uniform in two directions and describes its state only as a function of depth along the direction of the surface normal. In reality, PDRs have complex, wavy and corrugated surfaces. Due to limb brightening, the parts of the surface observed edge-on appear brighter. These edge-on observations are important because they provide direct observational access to the chemical stratification of the PDR, and hence, the stratification of the emission of different species. However, the curvature of the surface affects the observed spatial emission profiles, as the line of sight (LoS) passes through gas at different depths from the surface. This can distort the observed line profiles, hindering the accurate interpretation of observational data and the determination of physical parameters derived from PDR models. As observations of edge-on PDRs become more capable of resolving the stratification of emission, there is a growing demand for more advanced models that can directly compare the predicted spatial structure with such observations, instead of predictions based on infinite slab geometries.

One potential solution is to approximate the surface near the edge-on regions by its curvature radius. The simplest starting point for this approach is to map the 1D model to spherical geometry. Building on this concept, this project aims to develop a wrapper for MeudonPDR code that will compute observable spatial profiles of column densities on a spherical PDR surface and, preliminarily, line intensities by solving the radiative transfer along each LoS. To test the effectiveness of this method, the Horsehead Nebula serves as an ideal case study, as it is an edge-on PDR with available spatial emission data from several tracers.

This project is part of a collaboration between JPL (Darek Lis), Paris Observatory (us), IRAM (David Teyssier), and CSIC Madrid (Javier Goicoechea) to study the presence of water in the Horsehead Nebula. More generally, we aim to explain the localization of several emission lines, including  $\text{H}_2\text{O}$ , C,  $^{12}\text{CO}$ ,  $^{13}\text{CO}$ , and  $^{18}\text{CO}$  in the Horsehead.

The report is organized as follows: Sec. 2 describes the observational data used in this study. Sec. 3 outlines the methods. Specifically, in Sec. 3.1, I provide an overview of the MeudonPDR models, with Secs. 3.1.1, 3.1.2, and 3.1.3 describing how model parameters are determined, including comparisons between constant density and constant pressure models, the effects of the exact method of radiative transfer, and the effects of surface chemistry, respectively. In Sec. 3.2, I describe how column densities are computed for a spherical PDR surface. Sec. 3.3 discusses the solution of the radiative transfer equation along the LoS. Sec. 3.4 outlines the process of convolving model outputs with instrumental resolution. Sec. 4 presents the results, with Sec. 4.1 focusing on the convolved column densities, Sec. 4.2 on the effects of varying cloud radius, and Sec. 4.3 on the preliminary results of considering radiative transfer. Finally, Sec. 5 summarizes the conclusions and discusses the prospects of the study.

## 2 Data

The observational data used in this study (Fig. 3) were obtained from two instruments: the Heterodyne Instrument for the Far-Infrared (HIFI) (de Graauw et al. 2010) onboard the

Herschel Space Observatory (Pilbratt et al. 2010), and the IRAM-30m telescope (Baars et al. 1987). These data were taken along a cut through the Horsehead Nebula and were provided by Darek Lis. For consistency, all spatial profiles were convolved to a common spatial resolution of 38.1 arcsec, the resolution of the HIFI H<sub>2</sub>O observation, which has the lowest resolution among the observed lines. The molecular species observed, including H<sub>2</sub>O, C, <sup>12</sup>CO, and <sup>18</sup>CO, were detected at specific wavelengths corresponding to the transitions listed in Table. 1.

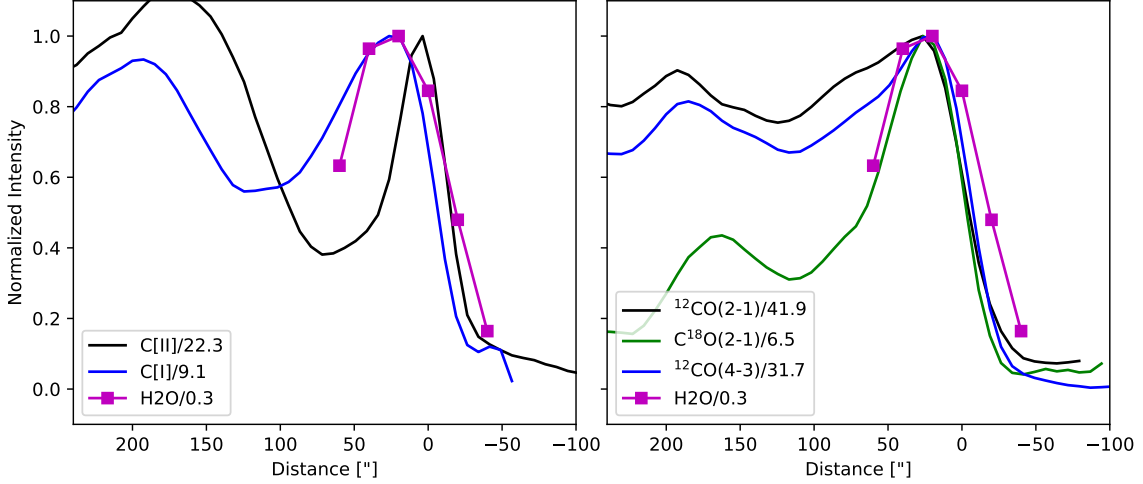


Figure 3: Observed line profiles of the Horsehead Nebula obtained with Herschel HIFI. Data provided by Darek Lis.

Notation	Species	Upper Level	Lower Level	Frequency (GHz)
H <sub>2</sub> O	H <sub>2</sub> O	J=1, Ka=1, Kc=0	J=1, Ka=0, Kc=1	557.30
C[II]	C <sup>+</sup>	2P J=3/2	2P J=1/2	1902.59
C[I]	C	3P J=1	3P J=0	492.02
<sup>12</sup> CO (2-1)	CO	v=0, J=2	v=0, J=1	230.538
<sup>12</sup> CO (4-3)	CO	v=0, J=4	v=0, J=3	461.041
C <sup>18</sup> O (2-1)	C <sup>18</sup> O	v=0, J=2	v=0, J=1	219.560

Table 1: Parameters of transitions in the observation data used in this study.

## 3 Methods

### 3.1 The MeudonPDR code

A significant heterogeneity exists among the available PDR models, which differ in their geometry, physical and chemical structures, and model parameters. Röllig et al. (2007) suggest that the choice of a specific code should depend on the physical and chemical processes implemented in the code, as well as the characteristics of the emission source.

In this project, I used the MeudonPDR code (Bron 2014; Bron et al. 2014, 2016; Goicoechea and Le Bourlot 2007; Gonzalez Garcia et al. 2008; Le Bourlot et al. 2012; Le Petit et al. 2006) to simulate the Horsehead Nebula. The MeudonPDR code models a stationary, 1D slab of gas and dust illuminated by a UV radiation field from one or both

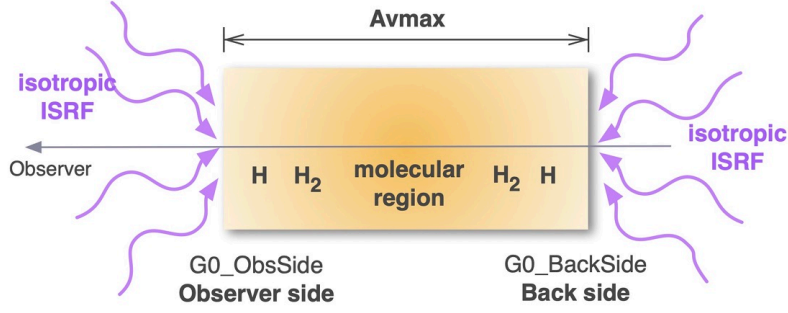


Figure 4: Scheme of the slab geometry in MeudonPDR code.  $A_V = 0$  at the observer side and increases toward the back side, reaching  $A_V = A_{V,\max}$ , which controls the size of the cloud. Reprinted from Fig. 3.1 in [MeudonPDR](#) documentation.

sides (Fig. 4). At each iteration, the code self-consistently solves the radiative transfer in both lines and continuum (from the UV to the radio domain), the chemical balance, the statistical equilibrium for level populations, and the thermal balance, all of which are deeply coupled to one another. The code outputs the level populations, gas temperature, and chemical abundances as a function of depth into the cloud, with optional output of the radiation field. The physical parameters used to model the Horsehead PDR are summarized in Table. 2.

Cloud size ( $A_{V,\max}^{(1)}$ )	40
Proton density <sup>(2)</sup> ( $n_H$ )	$3 \times 10^4 - 3 \times 10^6 \text{ cm}^{-3}$
Pressure <sup>(2)</sup> ( $P$ )	$1 \times 10^6 - 1 \times 10^7 \text{ K cm}^{-3}$
ISRF	shape: Mathis <sup>(3)</sup> , geometry: beam_isot <sup>(4)</sup>
ISRF scaling factor	$G_0^{\text{obs}} = 100$ , $G_0^{\text{back}} = 0.04^{(5)}$
UV radiative transfer method	FGK approximation, or exact H <sub>2</sub> self- and mutual shielding <sup>(6)</sup>
Turbulent velocity dispersion	$2 \text{ km s}^{-1(7)}$
Extinction Curve	HD38087 <sup>(8)</sup>
$R_V = A_V/E(B - V)^{(9)}$	5.50
$C_D = N_H/E(B - V)^{(9)}$	$1.57 \times 10^{22}$

Table 2: Key physical parameters used to model the Horsehead PDR in the MeudonPDR code.<sup>(1)</sup>Total visual extinction of the slab,  $A_V \equiv 2.5 \log_{10}(I_V^0/I_V^{\text{obs}})$ . <sup>(2)</sup>Proton density is used in constant density models, and pressure is used in constant pressure models (see Sec. 3.1.1). <sup>(3)</sup>Radiation field shape from Mathis et al. (1983). <sup>(4)</sup>ISRF geometry: beam perpendicular on the observer side, isotropic on the back side. <sup>(5)</sup>ISRF scaling factors are in Habing units, as defined in Le Petit et al. (2006). <sup>(6)</sup>UV radiative transfer methods include the FGK approximation or exact H<sub>2</sub> shielding (see Sec. 3.1.2). <sup>(7)</sup>Turbulent velocity dispersion is used only for Doppler line broadening. <sup>(8)</sup>Extinction curve from Fitzpatrick and Massa (1990). <sup>(9)</sup>Parameters related to extinction. Other parameters use default values. More descriptions can be found in the [MeudonPDR](#) documentation.

In a complex model such as the MeudonPDR code, different levels or types of approximations are possible. It is therefore necessary to decide what is adequate for this study. In the following sections, I investigate the impact of three of the most important choices on the PDR structure. First, since the code does not solve the hydrodynamics of the gas, either a constant pressure or a constant density profile must be assumed. Second, the modeling of H<sub>2</sub> self-shielding and the shielding of CO by H<sub>2</sub> is examined. The FGK



approximation, which treats each line independently in the UV transfer and neglects overlaps between absorption lines of  $\text{H}_2$  or between lines of  $\text{H}_2$  and other species such as  $\text{CO}$ , is compared to the “exact” transfer approach, which fully accounts for these overlaps. Finally, the inclusion of surface chemistry is considered. By default, the MeudonPDR code includes surface chemistry only for  $\text{H}_2$  formation, as surface processes often have little impact on some other PDR tracers. However, whether surface chemistry is significant for this study remains to be verified.

### 3.1.1 Constant Pressure vs. Constant Density

The density structure of a PDR model, whether it assumes constant density, constant pressure, or a user-defined density profile, can significantly influence the simulation results (Wolfire et al. 2022). As shown in Fig. 5 and Fig. 6, I compare the cloud structure computed with constant pressure and constant density assumptions, illustrating the differences in the resulting PDR structures. The values  $n_{\text{H}} = 3 \times 10^5 \text{ cm}^{-3}$  for the constant density model and  $P = 5 \times 10^6 \text{ K cm}^{-3}$  for the constant pressure model are based on Maillard (2023).

The PDR structure as a function of  $A_V$  in the constant density and constant pressure models differs most in the behavior of carbon and water near the  $\text{H}/\text{H}_2$  transition (Fig. 5), due to the much higher density in the constant density model. Additionally, the temperature in the atomic region is higher in the constant density model than in the constant pressure model. This occurs because, in the constant density model, the surface layer is much denser and absorbs UV radiation more efficiently. In contrast, in the constant pressure model (fixed  $P = nkT$ ), the density increases gradually from the surface to deeper regions as the temperature decreases. Consequently, in physical distance (Fig. 6), the constant pressure model has a more extended atomic region and a more compressed molecular region.

Observations of the Horsehead Nebula reveal a steep density gradient in the PDR (Guzmán et al. 2011; Habart et al. 2005). Hernández-Vera et al. (2023) showed that constant density models fail to reproduce the observed structures, and neither do previously proposed density profile prescriptions. Furthermore, recent observations from ALMA and Herschel indicate that the warm layer of PDRs is indeed isobaric, with relatively high thermal pressures (Bron et al. 2018; Goicoechea et al. 2016; Joblin et al. 2018; Maillard et al. 2021; Marconi et al. 1998; Wu et al. 2018). Based on these findings, I adopt a constant pressure model with  $P = 5 \times 10^6 \text{ K cm}^{-3}$  for the subsequent analysis.

### 3.1.2 Models with Exact Radiative Transfer of $\text{H}_2$

There are two options available in the MeudonPDR code for treating radiative transfer in the UV. The first is the FGK approximation (Federman et al. 1979), in which the self-shielding of  $\text{H}$  and  $\text{H}_2$  molecules is treated approximately. Self-shielding occurs when molecules absorb radiation in their own spectral lines, reducing the flux available to penetrate deeper into the cloud. However, the FGK approximation neglects mutual shielding, where the overlap and interaction of absorption lines between different species or multiple lines of the same species further attenuate the radiation field.

The second, more accurate approach is to solve the radiative transfer exactly, i.e., on a wavelength grid fine enough to resolve the multiple UV absorption lines of important species such as  $\text{H}$ ,  $\text{H}_2$ , and  $\text{CO}$ . This method explicitly includes mutual shielding for absorption lines corresponding to a given number of energy levels of  $\text{H}$ ,  $\text{H}_2$ ,  $\text{D}$ ,  $\text{HD}$ ,  $\text{CO}$ ,  $^{13}\text{CO}$ , and  $\text{C}^{18}\text{O}$ , as detailed in Goicoechea and Le Boulot (2007) and Gonzalez

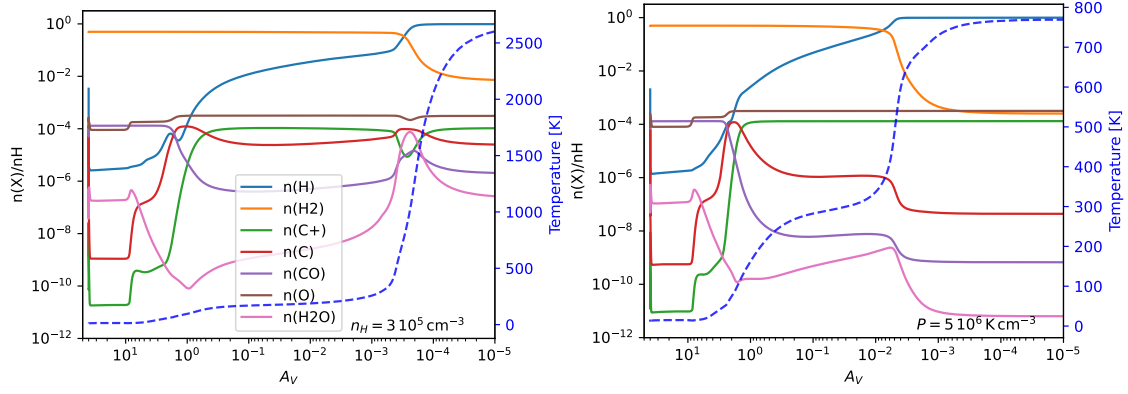


Figure 5: Comparison of the cloud structure computed with constant density  $n_H = 3 \times 10^5 \text{ cm}^{-3}$  (left) and constant pressure  $P = 5 \times 10^6 \text{ K cm}^{-3}$  (right), with a shared legend displayed in the left plot. The blues represent temperature and correspond to the right axes. All other parameters are the same as those listed in Table 2. Note that the radiation field is now coming from the right to conform with the observation, so  $A_V$  increases from right to left.

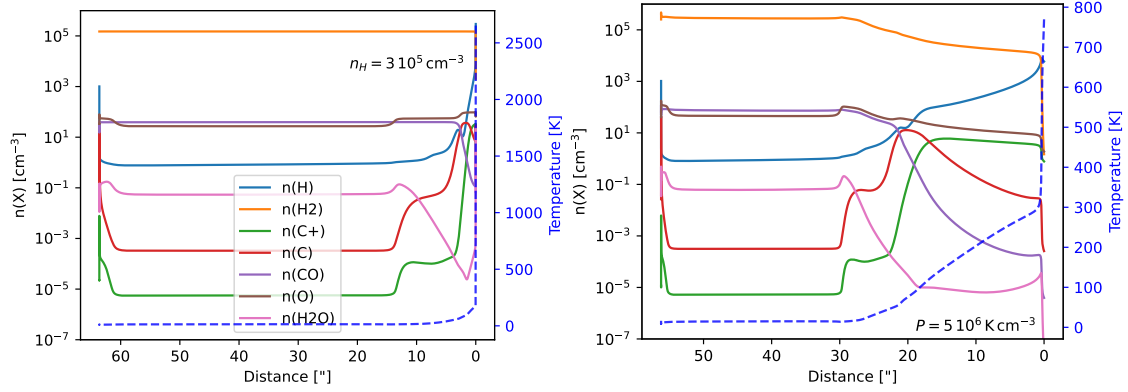


Figure 6: Similar to Fig. 5, but using physical units, with arcseconds as the distance unit and the densities represented by their actual values (not normalized by proton density).

Garcia et al. (2008). For higher energy levels, the FGK approximation is retained, as their contributions are negligible due to their low populations.

Fig. 7 compares spectra from  $1074 \text{ \AA}$  to  $1080 \text{ \AA}$  at various visual extinction values for models computed using the FGK approximation and the exact radiative transfer method, demonstrating pronounced attenuation when applying the exact method of  $\text{H}_2$  radiative transfer. Although computationally more intensive, the exact method enables a more accurate treatment of the UV radiation field, which subsequently influences the PDR structure. For instance, the exact method leads to increased attenuation of the radiation field, shifting the  $\text{H}/\text{H}_2$  transition layer to lower extinction depths (Goicoechea and Le Boulrot 2007), as illustrated in Fig. 8. Furthermore, the enhanced attenuation from mutual shielding results in a lower temperature profile. To balance accuracy and computational efficiency, my model applies exact radiative transfer only to the 20 lowest energy levels of  $\text{H}_2$ , which are the primary contributors to the attenuation.

### 3.1.3 Models with Surface Chemistry

In the ISM, direct gas-phase formation of molecules is inefficient for some molecules. Instead, molecules are formed on the surfaces of dust grains, which act as catalysts by providing a surface for adsorbed atoms to meet and react. The grains also absorb the excess

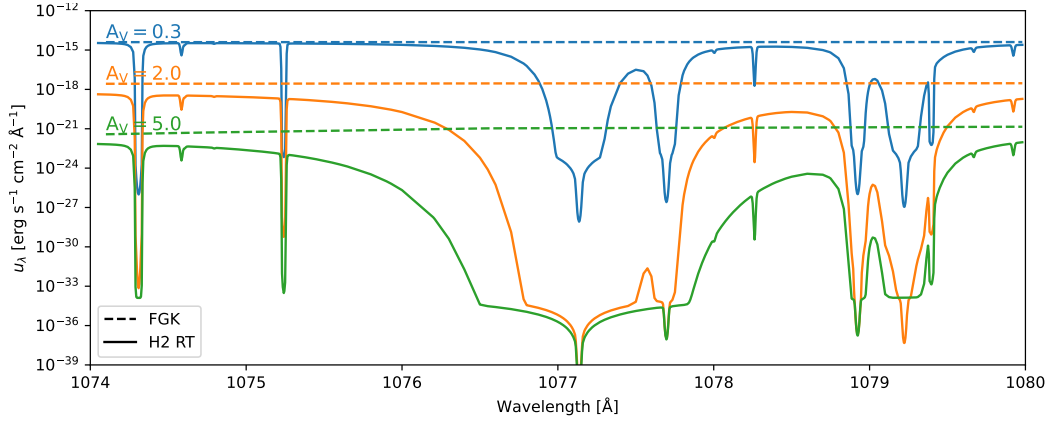


Figure 7: Comparison of the local energy density of the radiation field from 1074 Å to 1080 Å at visual extinction depths  $A_V = 0.3$  (blue),  $A_V = 2$  (orange), and  $A_V = 5$  (green), for models computed using the FGK approximation (dashed lines) and the exact radiative transfer method (solid lines) including the 20 lowest  $H_2$  absorption lines.

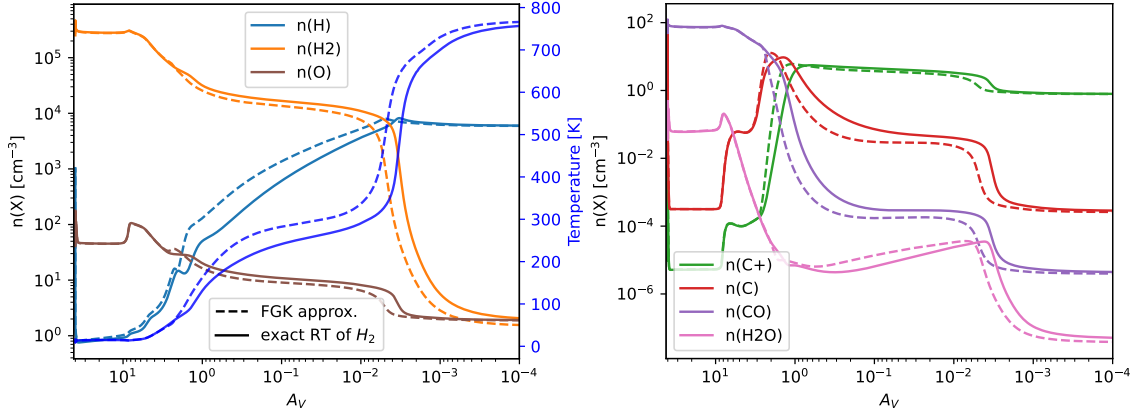


Figure 8: Comparison of temperature profile and abundances for models computed with exact radiative transfer (solid lines) and FGK approximation (dashed lines) for  $H_2$  UV lines: H species and O (left), and C, CO, and  $H_2O$  (right).

energy released by the formation process, preventing dissociation that would otherwise occur in the gas-phase formation. The formation of  $H_2$  is a key demonstration of the importance of this process, as the gas-phase formation rate of  $H_2$  is much lower than the rate required to explain the observed abundance of  $H_2$  in the ISM (Gould and Salpeter 1963; Hollenbach and Salpeter 1971). In addition to chemical reactions, dust grains also play a role in the sublimation and freeze-out of molecules, leading to the sudden apparition or disparition of some molecules at depths where the dust temperature crosses specific threshold values (Herbst and van Dishoeck 2009).

In Fig. 9, I compare the PDR models computed with and without surface chemistry. As previously noted,  $H_2$  formation on grains is by default included in both models. The inclusion of surface reactions leads to a substantial earlier rise in the abundances of  $n(CO)$  and  $n(H_2O)$  due to enhanced production on dust grain surfaces. At greater depths within the cloud, the abundances of almost all molecules decrease in the model with surface chemistry because of the freeze-out of molecules onto the dust grains. Grains also reduce the gas temperature, as the abundances of key coolants, such as CO and  $H_2O$ , increases, as shown in the left panel. Since CO and  $H_2O$  are present in the observations we aim to study, it is crucial to include surface chemistry in the models.

As a result of the model comparisons in this section, all models run in this project will

use a constant pressure prescription, exact radiative transfer for H<sub>2</sub> UV lines, and surface chemistry.

### 3.2 Modeling Column Densities in a Spherical PDR

To model the curvature of the cloud, I treat the PDR as the outermost shell of a fictitious spherical cloud, as illustrated in Fig. 10. The radial profile of this PDR layer is approximated by the results of a 1D plane-parallel PDR model. This approximation is valid when the depth of the PDR is relatively small compared to the radius of the cloud. For the models in this study, the physical depth of the PDR is approximately 0.08 pc, which is significantly smaller than the curvature radius, as seen in Fig. 2, thereby justifying the use of the plane-parallel approximation. Consequently, all physical variables at a given distance from the cloud's surface are considered as equivalent to those computed by the MeudonPDR model at the same distance from the cloud's edge.

The radius  $R$  of the fictitious spherical cloud is provided as an input parameter to the wrapper code. A LoS is defined by its impact parameter  $b$ , which measures the perpendicular distance from the LoS to the center of the cloud. From the output of the MeudonPDR code, the level number densities  $n_X(d)$  are obtained as a function of the depth  $d$  into the cloud. In plane-parallel geometry,  $n_X(d)$  gives the number density at a point located at a depth  $d$  from the spherical surface.

The column density along a given LoS is determined by interpolating the number density at any depth  $d$  and then integrating along the LoS. To do this, I first compute the range of distances inside the PDR region along the LoS. The maximum half-distance  $s_{\max}$  is given by:

$$s_{\max} = \sqrt{R^2 - b^2}, \quad (2)$$

while the computation of the minimum half-distance  $s_{\min}$  depends on whether the LoS penetrates beyond the PDR region (see the right panel of Fig. 10):

$$s_{\min} = \begin{cases} 0 & \text{if } b > R - d_{\text{PDR}}, \text{ LoS 1} \\ \sqrt{(R - d_{\text{PDR}})^2 - b^2} & \text{if } b < R - d_{\text{PDR}}, \text{ LoS 2} \end{cases}, \quad (3)$$

where  $d_{\text{PDR}}$  is the depth of the PDR region. Next, the distance  $s$  along the LoS is converted into the depth  $d$  from the cloud's surface. Using Pythagorean theorem, one can easily establish that  $d = R - \sqrt{s^2 + b^2}$ . The number density at each point along the LoS is then

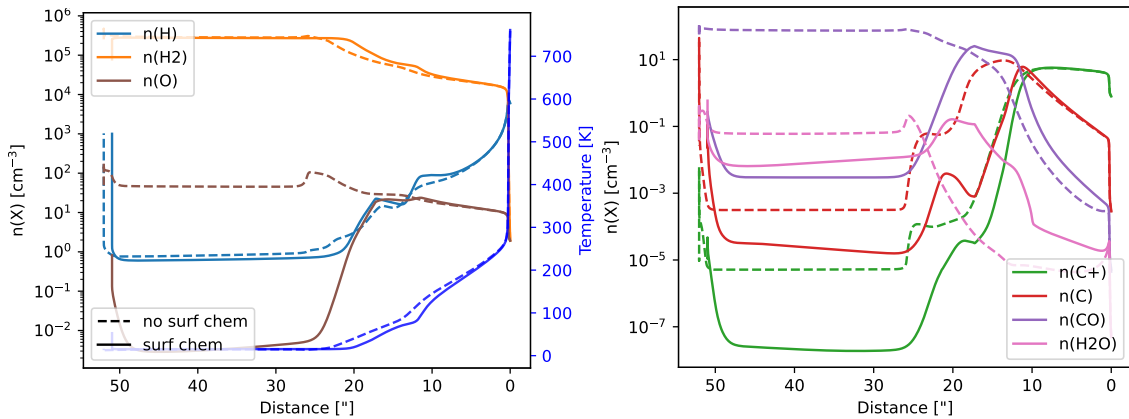


Figure 9: Comparison of temperature profile and abundances for models computed with (solid lines) and without (dashed lines) surface chemistry: H species and O (left), and C, CO, and H<sub>2</sub>O (right).

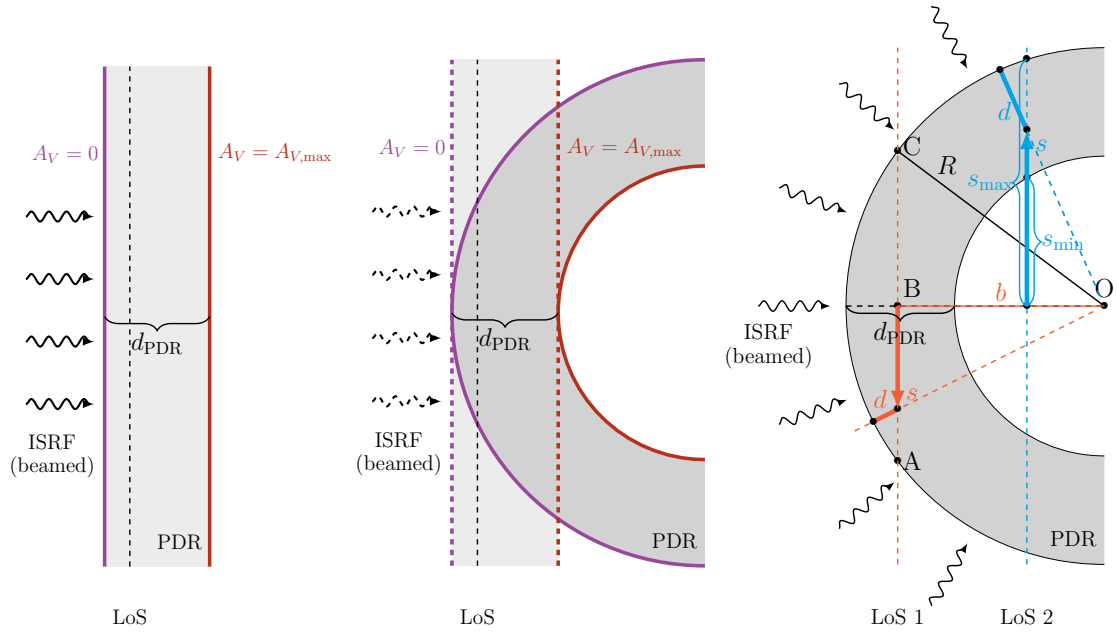


Figure 10: Scheme of the slab geometry in MeudonPDR code (left), the transformation from slab to spherical geometry (middle), and the spherical PDR layer with the definition of the different distances used in the text (right). The purple line represents the illuminated front of the PDR, while the red line represents the backside. When transforming from slab geometry to spherical geometry, the beamed ISRF remains perpendicular to the surface. The curvature is exaggerated for clarity.

calculated as:

$$n_X(s) = f(R - \sqrt{s^2 + b^2}), \quad (4)$$

where  $f(d)$  is the interpolated function of the level number density  $n_X(d)$ . Finally, the column density  $N_X(b)$  for a given LoS with impact parameter  $b$  is obtained by integrating the number density along the LoS. By symmetry, the total column density is twice the integral over the half-LoS:

$$N_X(b) = 2 \int_{s_{min}}^{s_{max}} n_X(s') ds'. \quad (5)$$

By considering the curvature of the cloud's surface, this column density allows for a more direct comparison with observations. However, this approach does not account for the absorption processes occurring inside the cloud. For lines that are optically thick, the radiative transfer equation must be solved along the LoS to accurately reproduce the observed line profiles. This more detailed treatment will be addressed in the next section.

### 3.3 Solving the Radiative Transfer Equation

The column densities are useful when the lines are optically thin, as they are proportional to the line intensities in this case. However, some lines can be optically thick, leading to differences in the observed spatial profiles for various lines, as seen in Fig. 3. In such cases, a more detailed treatment is required to account for line reabsorption within the cloud. To achieve this, I need to solve the radiative transfer equation along the LoS (see, e.g., Rybicki and Lightman 1979, Eq. 1.67):

$$\frac{dI_\nu}{ds} = A_{ul}n_u \frac{h\nu}{4\pi} \phi(\nu) + B_{ul}n_u \frac{h\nu}{4\pi} I_\nu \phi(\nu) - B_{lu}n_l \frac{h\nu}{4\pi} I_\nu \phi(\nu), \quad (6)$$

where  $n_u$  and  $n_l$  are the number densities of the upper and lower levels of the transition, respectively,  $h$  is the Planck's constant,  $\nu$  is the frequency of the transition, and  $\phi(\nu)$  is the line profile. I assume that the line profile is dominated by turbulent broadening, with a constant turbulent velocity dispersion throughout the cloud. Dust is neglected, as its cross sections are relatively low in the far-infrared (FIR) and submillimeter domains.

The coefficients  $A_{ul}$ ,  $B_{ul}$ ,  $B_{lu}$  in Eq. 6 are the Einstein coefficients for spontaneous emission, stimulated emission, and absorption, respectively. These coefficients are intrinsic properties of the specific transition and are related through the Einstein relations (Einstein 1917):

$$B_{ul} = \frac{c^2}{2h\nu_{ul}^3} A_{ul}, \quad g_l B_{lu} = g_u B_{ul}, \quad (7)$$

where  $g_u$  and  $g_l$  are the degeneracies of the upper and lower levels.

In PDRs, the motion of atoms and molecules results in line broadening. Thermal motion produces a Gaussian profile, while microturbulent motions contribute an additional broadening component. The thermal and turbulent broadening effects are combined in the effective Doppler width,  $\Delta\nu_D$ , which is then included in the Gaussian line profile (see, e.g., Rybicki and Lightman 1979, Eqs. 10.68-10.72):

$$\phi(\nu) = \frac{1}{\sigma_\nu \sqrt{2\pi}} \exp\left(-\frac{(\nu - \nu_0)^2}{2\sigma_\nu^2}\right), \quad (8)$$

where

$$\sigma_\nu = \frac{\sqrt{2}}{2} \Delta\nu_D, \quad \Delta\nu_D = \frac{\nu_0}{c} \sqrt{\frac{2kT}{m} + v_{\text{turb}}^2}. \quad (9)$$

Here,  $\nu_0$  is the central frequency of the transition,  $c$  is the speed of light,  $T$  is the gas temperature,  $m$  is the mass of the emitting species, and  $v_{\text{turb}} = 2 \text{ km s}^{-1}$  is the turbulent velocity, as introduced in Table. 2.

The line profile is normalized so that  $\int_0^\infty \phi(\nu) d\nu = 1$ . To ensure computational efficiency while maintaining a good representation of the profile, I truncate the line profile at  $5\sigma$ . Therefore, in practice, the normalization becomes  $\int_{\nu_0-5\sigma}^{\nu_0+5\sigma} \phi(\nu) d\nu = 1$ .

To solve the radiative transfer equation, I also need a background intensity  $I_0$ . In the PDR model, the external radiation field includes a component from the IR/FIR due to dust emission from the surroundings of the PDR. I use this as the background intensity for the radiative transfer calculation.

The external radiation field in the `IncRadField.dat` file is provided in units of  $\text{erg/cm}^2/\text{s}/\text{sr}/\text{\AA}$ . However, to solve the radiative transfer equation, I need the specific intensity in units of  $\text{erg/cm}^2/\text{s}/\text{sr}/\text{Hz}$ . By energy conservation,  $I_\nu |d\nu| = I_\lambda |d\lambda|$ , and using  $c = \lambda\nu$ , I can derive the differential relation  $d\lambda = -c/\nu^2 d\nu$ . This allows me to convert between the two quantities as follows:

$$I_\nu = I_\lambda \left| \frac{d\lambda}{d\nu} \right| = I_\lambda \frac{c}{\nu^2} = I_\lambda \frac{\lambda^2}{c}. \quad (10)$$

Thus far, I have focused on improving the geometry of PDR models. However, the observed spectra are inevitably influenced by the resolution of the instrument used for observation. The instrumental resolution smooths out the line spatial profile, broadening the observed lines and altering their shapes. Consequently, it is essential to account for the instrument's resolution in the modeling process. In the following section, I will discuss the convolution process and how it modifies the observed spectra.



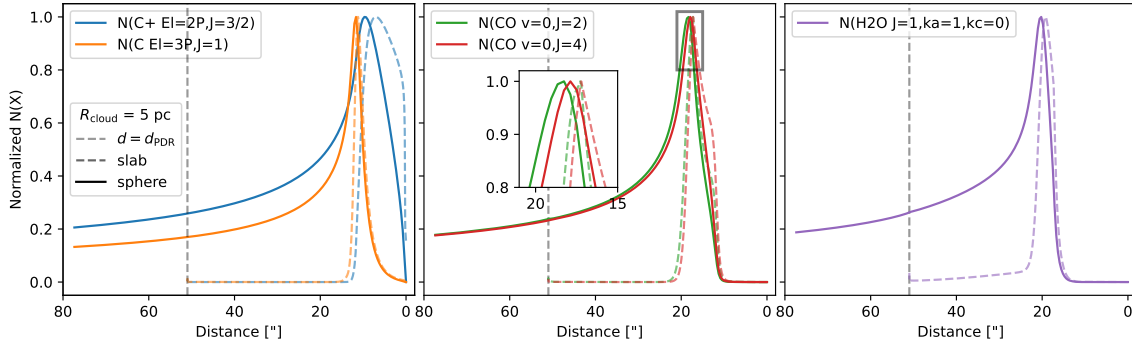


Figure 11: Comparison of normalized column density profiles for slab geometry (dashed lines) and spherical geometry (solid lines) with a cloud radius of  $R_{\text{cloud}} = 5$  pc. In Panel 1,  $N(\text{C}^+ 2\text{P}, J=3/2)$  (blue) and  $N(\text{C } 3\text{P}, J=1)$  (orange) are shown; in Panel 2,  $N(\text{CO } v=0, J=2)$  (green) and  $N(\text{CO } v=0, J=4)$  (red); and in Panel 3,  $N(\text{H}_2\text{O } J=1, k_a=1, k_c=0)$  (purple). The dashed gray lines indicate the maximum depth of the PDR model,  $d_{\text{PDR}}$ . The rectangle marks the zoomed-in region in Panel 2.

### 3.4 Convolution of Line Profiles with Instrumental Resolution

The spatial resolution of an instrument is typically characterized by its point spread function (PSF), which describes the response of the instrument to a point source. To account for the effects of instrumental resolution on the observed line profiles, I convolve the model's line profile with the PSF. Since the spatial grid provided by MeudonPDR code is non-uniform, I first interpolate it onto a uniform and monotonic grid.

The PSF is often approximated as a Gaussian function. For this work, the Gaussian kernel is expressed as:

$$g(x) = \frac{1}{\sigma\sqrt{2\pi}} \exp\left(-\frac{x^2}{2\sigma^2}\right), \quad (11)$$

where  $x$  is the distance from the center of the PSF, and  $\sigma$  is the standard deviation of the Gaussian. The standard deviation  $\sigma$  is related to the full width half maximum (FWHM) of the instrument by  $\sigma = \text{FWHM} / (2\sqrt{2 \ln 2})$ .

To reduce computational cost, I truncate the Gaussian PSF at  $3\sigma$ , as the contribution from points beyond this range is negligible. The PSF is then normalized over the truncated range to conserve total intensity, with the normalization constant  $K = \sum_{x=-3\sigma}^{3\sigma} g(x)\Delta x$ , where  $\Delta x$  is the spacing of the uniform grid.

The convolution of the line profile,  $f(x)$ , with the normalized PSF is performed as:

$$(f * g)(x) = \frac{1}{K} \sum_{\tau=x_{\min}-3\sigma}^{x_{\max}+3\sigma} F(\tau)g(x-\tau)\Delta x, \quad (12)$$

where  $x_{\min}$  and  $x_{\max}$  define the bounds of the spatial grid, and  $F(\tau)$  is the value of the line profile at point  $\tau$ .

## 4 Results and Discussion

### 4.1 Convolved Column Densities from Spherical Model

In Secs. 3.2 and 3.4, I described the modeling of spherical geometry using the wrapper for the MeudonPDR code and the convolution of line profiles with the instrumental

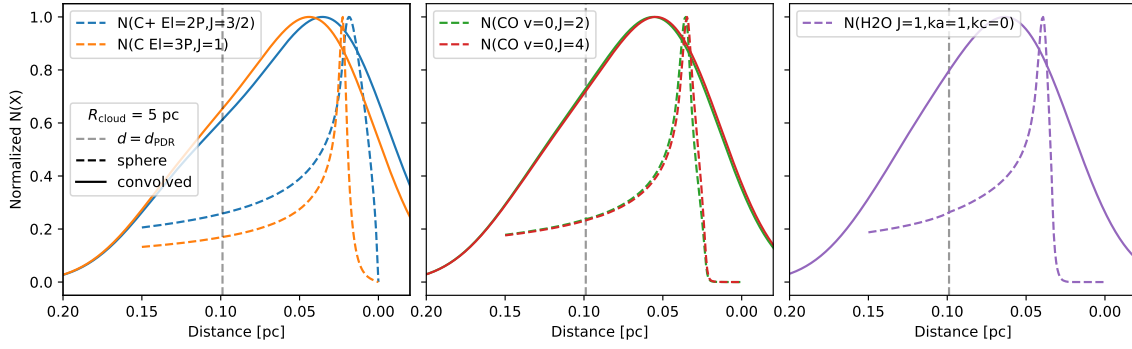


Figure 12: Similar to Fig. 11, but showing the comparison between unconvolved (dashed lines) and convolved (solid lines) column densities.

resolution. In this section, I present the convolved column density profiles for the spherical geometry model with a cloud radius of  $R_{\text{cloud}} = 5$  pc. Comparisons are made first between the spherical and slab geometry models, then between the unconvolved and convolved profiles, and finally between the convolved profiles and the observational data.

Fig. 11 compares the profiles from the spherical geometry model with those from the slab geometry models. In the spherical geometry model, the curvature of the cloud’s surface causes the PDR layer to bend away from the tangent at the cloud’s surface, in contrast to the slab geometry, where the PDR layer is directly at the surface. As a result, the PDR layer reaches greater depths in the spherical geometry, producing a more extended profile. Additionally, the peaks shift to deeper locations within the cloud, as the line of sight (LoS) passing through the greatest distance within the emitting region is slightly behind the emitting region. When convolution with instrument resolution is applied, the line profiles are smoothed and further extended (Fig. 12), with the peaks shifting to greater depths. The convex tail behind the emitting region disappears, yielding a more Gaussian-like shape.

The convolved profiles provide a better match to the observed data, as shown in Fig. 13, particularly in terms of the shape and extent of the profiles. The peak widths are relatively consistent with the observations, and with spherical geometry, we begin to observe an asymmetry in the spatial profiles. This suggests that including curvature and convolution improves the modeling of the observed column density profiles. However, except for  $\text{C}^+$ , the asymmetry does not align well with the observed profiles. Moreover, the shift between  $\text{C}^+/\text{C}$  and the earlier peak of  $\text{H}_2\text{O}$  in the observations are not reproduced by the models. A possible explanation for this discrepancy could be the cloud radius, which is a free parameter in the model. In the following section, I will explore how varying the cloud radius affects the column density profiles.

## 4.2 Effect of Cloud Radius on Column Densities

There are no significant changes to the rising side of the profiles or the locations of the peaks with varying cloud radius  $R_{\text{cloud}}$ . Instead, variations in  $R_{\text{cloud}}$  primarily affect the shape of the profile’s tail (Fig. 14). As the cloud radius increases, the surface curvature decreases, making the emitting region more tangent to the LoS at the same depth from the cloud’s surface. This reduces the passage length and, consequently, causes the tail to decline more steeply.

None of the models reproduce the observed profiles accurately. A direct comparison, with profiles overlapped to emphasize differences in shape, is provided in Fig. 17 in the appendix. Notably, the observed profiles exhibit significant variation in the tail shape,

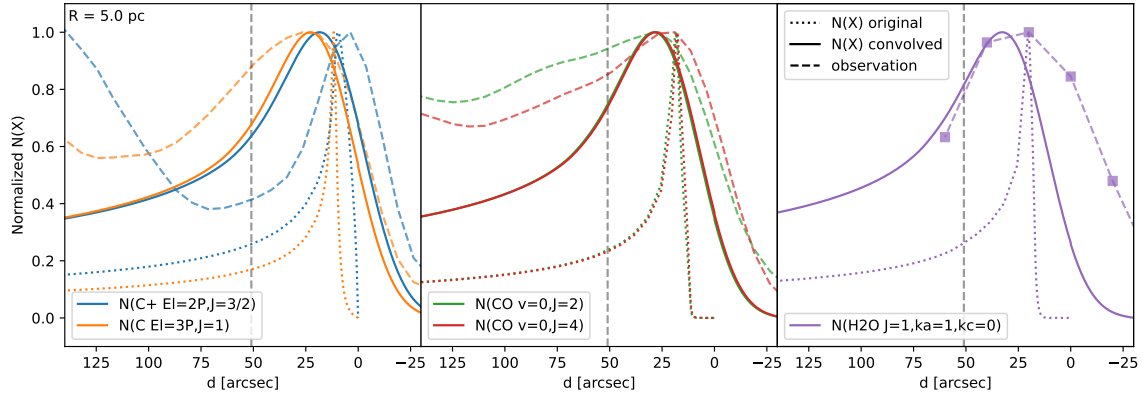


Figure 13: Comparison of column density profiles for a model with spherical geometry ( $R_{\text{cloud}} = 5 \text{ pc}$ , solid lines) and observations (dashed lines). The unconvolved profiles (dotted lines) are also shown for comparison.

whereas the modeled profiles remain quite similar. This discrepancy is likely due to the lack of a detailed treatment of radiative transfer along the LoS, as mentioned in Sec. 3.3, which I will address in the next section.

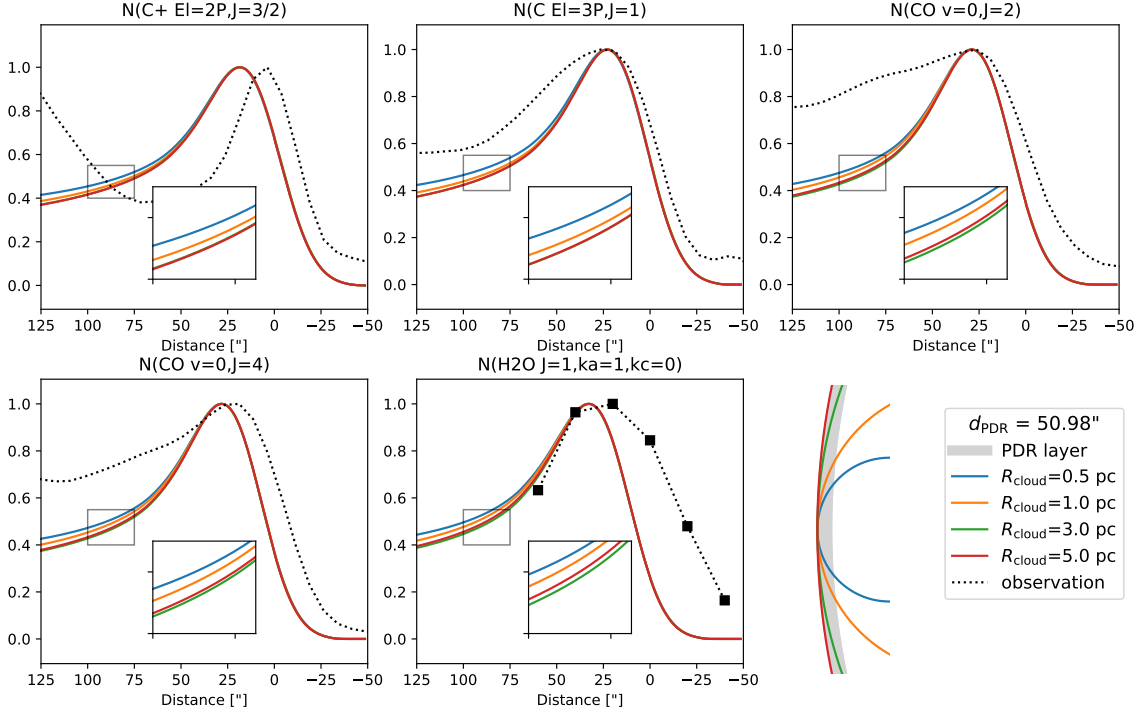


Figure 14: Comparison of normalized line profiles for different cloud radii:  $R_{\text{cloud}} = 0.5 \text{ pc}$  (blue),  $1.0 \text{ pc}$  (orange),  $3.0 \text{ pc}$  (green), and  $5.0 \text{ pc}$  (red). Observations are shown as dotted lines. A schematic representation of the cloud radii is included in the bottom right corner. The areas marked by black rectangles are shown with greater detail in zoomed-in views.

### 4.3 Line Profiles with Radiative Transfer

To validate the solver, I test it by solving the radiative transfer equation with constant density profiles for both the lower and upper levels, for which an analytical solution can

be obtained. In this case, the radiative transfer equation simplifies to:

$$\frac{dI_\nu}{ds} = c_1 + c_2 I_\nu, \quad (13)$$

where  $c_1 = A_{ul}n_u\phi(\nu)h\nu/4\pi$  and  $c_2 = (B_{ul}n_u - B_{lu}n_l)\phi(\nu)h\nu/4\pi$  are constants. The analytical solution to this equation is:

$$I_\nu(s) = (I_0 + \frac{c_1}{c_2})e^{c_2 s} - \frac{c_1}{c_2}. \quad (14)$$

For this toy problem, I solve the radiative transfer equation for the CO transition from  $v = 0, J = 2$  to  $v = 0, J = 1$ , assuming constant density profiles of  $n_u = 2 \text{ cm}^{-3}$  and  $n_l = 2 \text{ cm}^{-3}$ . The computed results are compared with the analytical solution in Fig. 15.

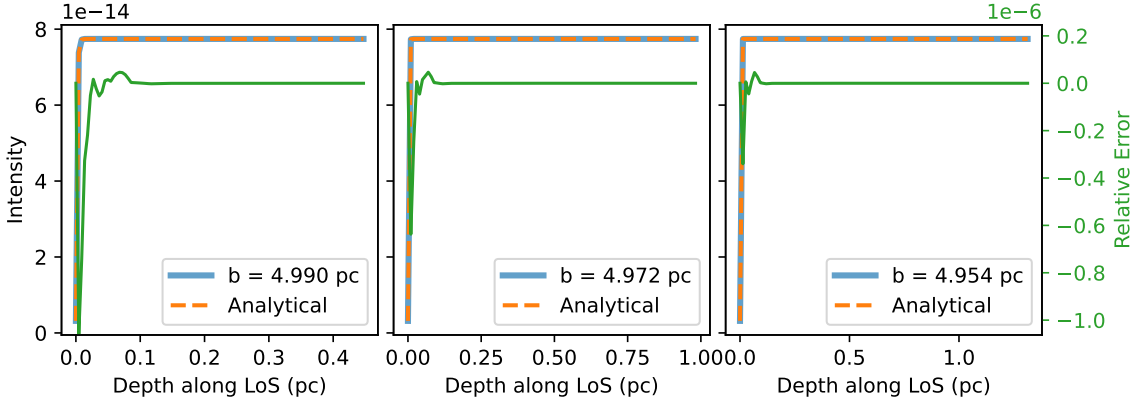


Figure 15: Comparison of the computed (blue solid lines) and analytical (orange dashed lines) solutions to the radiative transfer equation for the CO transition from  $v = 0, J = 2$  to  $v = 0, J = 1$  along LoS with different impact parameters in a 5 pc cloud. The right axes show the relative error of the numerical solution, defined as  $|I_\nu^{\text{num}} - I_\nu^{\text{ana}}|/I_\nu^{\text{ana}}$ .

Due to time constraints, I was unable to fully implement the method discussed in Sec. 3.3. Specifically, my results are limited to solving the radiative transfer equation at the line center, without taking into account the line-broadening profile,  $\phi(\nu)$ . Despite this limitation, the implemented methods illustrate how solving the radiative transfer equation along the LoS affects the shape of the profiles. Future work could build on these results by incorporating the full line-broadening profile and comparing the results with observed data.

## 5 Conclusions

## References

- Abergel, A. et al. (2003). “ISOCAM and molecular observations of the edge of the Horsehead nebula”. In: A&A 410, pp. 577–585. DOI: [10.1051/0004-6361:20030878](https://doi.org/10.1051/0004-6361:20030878).
- Baars, J. W. M. et al. (1987). “The IRAM 30-m millimeter radio telescope on Pico Veleta, Spain”. In: A&A 175.1-2, pp. 319–326.
- Bron, E. (2014). “Stochastic processes in the interstellar medium”. 2014PA077169. PhD thesis, 1 vol. (382 p.)
- Bron, E., Le Bourlot, J., and Le Petit, F. (2014). “Surface chemistry in the interstellar medium. II. H<sub>2</sub> formation on dust with random temperature fluctuations”. In: A&A 569, A100, A100. DOI: [10.1051/0004-6361/201322101](https://doi.org/10.1051/0004-6361/201322101).
- Bron, E., Le Petit, F., and Le Bourlot, J. (2016). “Efficient ortho-para conversion of H<sub>2</sub> on interstellar grain surfaces”. In: A&A 588, A27, A27. DOI: [10.1051/0004-6361/201527879](https://doi.org/10.1051/0004-6361/201527879).
- Bron, E. et al. (2018). “Photoevaporating PDR models with the Hydra PDR Code”. In: *arXiv e-prints*, arXiv:1801.01547, arXiv:1801.01547. DOI: [10.48550/arXiv.1801.01547](https://doi.org/10.48550/arXiv.1801.01547).
- Crawford, M. K. et al. (1985). “Far-infrared spectroscopy of galaxies : the 158 micron C+ line and the energy balance of molecular clouds.” In: ApJ 291, pp. 755–771. DOI: [10.1086/163113](https://doi.org/10.1086/163113).
- de Graauw, T. et al. (2010). “The Herschel-Heterodyne Instrument for the Far-Infrared (HIFI)”. In: A&A 518, L6, p. L6. DOI: [10.1051/0004-6361/201014698](https://doi.org/10.1051/0004-6361/201014698).
- Draine, B. T. (2011). *Physics of the Interstellar and Intergalactic Medium*.
- Einstein, A. (1917). “Zur Quantentheorie der Strahlung”. In: *Physikalische Zeitschrift* 18, pp. 121–128.
- Federman, S. R., Glassgold, A. E., and Kwan, J. (1979). “Atomic to molecular hydrogen transition in interstellar clouds.” In: ApJ 227, pp. 466–473. DOI: [10.1086/156753](https://doi.org/10.1086/156753).
- Fitzpatrick, E. L. and Massa, D. (1990). “An Analysis of the Shapes of Ultraviolet Extinction Curves. III. an Atlas of Ultraviolet Extinction Curves”. In: ApJS 72, p. 163. DOI: [10.1086/191413](https://doi.org/10.1086/191413).
- Goicoechea, J. R. and Le Bourlot, J. (2007). “The penetration of Far-UV radiation into molecular clouds”. In: A&A 467.1, pp. 1–14. DOI: [10.1051/0004-6361:20066119](https://doi.org/10.1051/0004-6361:20066119).
- Goicoechea, J. R. et al. (2016). “Compression and ablation of the photo-irradiated molecular cloud the Orion Bar”. In: Nature 537.7619, pp. 207–209. DOI: [10.1038/nature18957](https://doi.org/10.1038/nature18957).
- Gonzalez Garcia, M. et al. (2008). “Radiative transfer revisited for emission lines in photon dominated regions”. In: A&A 485.1, pp. 127–136. DOI: [10.1051/0004-6361:200809440](https://doi.org/10.1051/0004-6361:200809440).
- Gould, R. J. and Salpeter, E. E. (1963). “The Interstellar Abundance of the Hydrogen Molecule. I. Basic Processes.” In: ApJ 138, p. 393. DOI: [10.1086/147654](https://doi.org/10.1086/147654).
- Guzmán, V. et al. (2011). “H<sub>2</sub>CO in the Horsehead PDR: photo-desorption of dust grain ice mantles”. In: A&A 534, A49, A49. DOI: [10.1051/0004-6361/201117257](https://doi.org/10.1051/0004-6361/201117257).
- Habart, E. et al. (2005). “Density structure of the Horsehead nebula photo-dissociation region”. In: A&A 437.1, pp. 177–188. DOI: [10.1051/0004-6361:20041546](https://doi.org/10.1051/0004-6361:20041546).
- Herbst, E. and van Dishoeck, E. F. (2009). “Complex Organic Interstellar Molecules”. In: ARA&A 47.1, pp. 427–480. DOI: [10.1146/annurev-astro-082708-101654](https://doi.org/10.1146/annurev-astro-082708-101654).
- Hernández-Vera, C. et al. (2023). “The extremely sharp transition between molecular and ionized gas in the Horsehead nebula”. In: A&A 677, A152. DOI: [10.1051/0004-6361/202347206](https://doi.org/10.1051/0004-6361/202347206).
- Hollenbach, D. and Salpeter, E. E. (1971). “Surface Recombination of Hydrogen Molecules”. In: ApJ 163, p. 155. DOI: [10.1086/150754](https://doi.org/10.1086/150754).

- Joblin, C. et al. (2018). “Structure of photodissociation fronts in star-forming regions revealed by Herschel observations of high-J CO emission lines”. In: A&A 615, A129, A129. DOI: [10.1051/0004-6361/201832611](https://doi.org/10.1051/0004-6361/201832611).
- Le Bourlot, J. et al. (2012). “Surface chemistry in the interstellar medium. I. H<sub>2</sub> formation by Langmuir-Hinshelwood and Eley-Rideal mechanisms”. In: A&A 541, A76, A76. DOI: [10.1051/0004-6361/201118126](https://doi.org/10.1051/0004-6361/201118126).
- Le Petit, F. et al. (2006). “A Model for Atomic and Molecular Interstellar Gas: The Meudon PDR Code”. In: ApJS 164.2, pp. 506–529. DOI: [10.1086/503252](https://doi.org/10.1086/503252).
- Maillard, V. (2023). “Model of photo-evaporating fronts in star forming regions”. Theses. Université Paris sciences et lettres.
- Maillard, V., Bron, E., and Le Petit, F. (2021). “Dynamical effects of the radiative stellar feedback on the H I-to-H<sub>2</sub> transition”. In: A&A 656, A65, A65. DOI: [10.1051/0004-6361/202140865](https://doi.org/10.1051/0004-6361/202140865).
- Marconi, A. et al. (1998). “Near infrared spectra of the Orion bar”. In: A&A 330, pp. 696–710. DOI: [10.48550/arXiv.astro-ph/9710051](https://doi.org/10.48550/arXiv.astro-ph/9710051).
- Mathis, J. S., Mezger, P. G., and Panagia, N. (1983). “Interstellar radiation field and dust temperatures in the diffuse interstellar medium and in giant molecular clouds”. In: A&A 128, pp. 212–229.
- Menten, K. M. et al. (2007). “The distance to the Orion Nebula”. In: A&A 474.2, pp. 515–520. DOI: [10.1051/0004-6361:20078247](https://doi.org/10.1051/0004-6361:20078247).
- Pilbratt, G. L. et al. (2010). “Herschel Space Observatory. An ESA facility for far-infrared and submillimetre astronomy”. In: A&A 518, L1, p. L1. DOI: [10.1051/0004-6361/201014759](https://doi.org/10.1051/0004-6361/201014759).
- Röllig, M. et al. (2007). “A photon dominated region code comparison study”. In: A&A 467.1, pp. 187–206. DOI: [10.1051/0004-6361:20065918](https://doi.org/10.1051/0004-6361:20065918).
- Rybicki, G. B. and Lightman, A. P. (1979). *Radiative processes in astrophysics*.
- Schirmer, T. et al. (2020). “Dust evolution across the Horsehead nebula”. In: A&A 639, A144, A144. DOI: [10.1051/0004-6361/202037937](https://doi.org/10.1051/0004-6361/202037937).
- Schlafly, E. F. et al. (2014). “A Large Catalog of Accurate Distances to Molecular Clouds from PS1 Photometry”. In: ApJ 786.1, 29, p. 29. DOI: [10.1088/0004-637X/786/1/29](https://doi.org/10.1088/0004-637X/786/1/29).
- Stacey, G. J. et al. (2010). “A 158  $\mu\text{m}$  [C II] Line Survey of Galaxies at  $z \sim 1-2$ : An Indicator of Star Formation in the Early Universe”. In: ApJ 724.2, pp. 957–974. DOI: [10.1088/0004-637X/724/2/957](https://doi.org/10.1088/0004-637X/724/2/957).
- Tielens, A. G. G. M. and Hollenbach, D. (1985). “Photodissociation regions. I. Basic model.” In: ApJ 291, pp. 722–746. DOI: [10.1086/163111](https://doi.org/10.1086/163111).
- Warren Jr., W. H. and Hesser, J. E. (1977). “A photometric study of the Orion OB1 association. I. Observational data.” In: ApJS 34, pp. 115–206. DOI: [10.1086/190446](https://doi.org/10.1086/190446).
- Wolfire, M. G., Vallini, L., and Chevance, M. (2022). “Photodissociation and X-Ray-Dominated Regions”. In: *Annual Review of Astronomy and Astrophysics* 60. Volume 60, 2022, pp. 247–318. DOI: <https://doi.org/10.1146/annurev-astro-052920-010254>.
- Wu, R. et al. (2018). “Constraining physical conditions for the PDR of Trumpler 14 in the Carina Nebula”. In: A&A 618, A53, A53. DOI: [10.1051/0004-6361/201832595](https://doi.org/10.1051/0004-6361/201832595).



## Supplementary Material

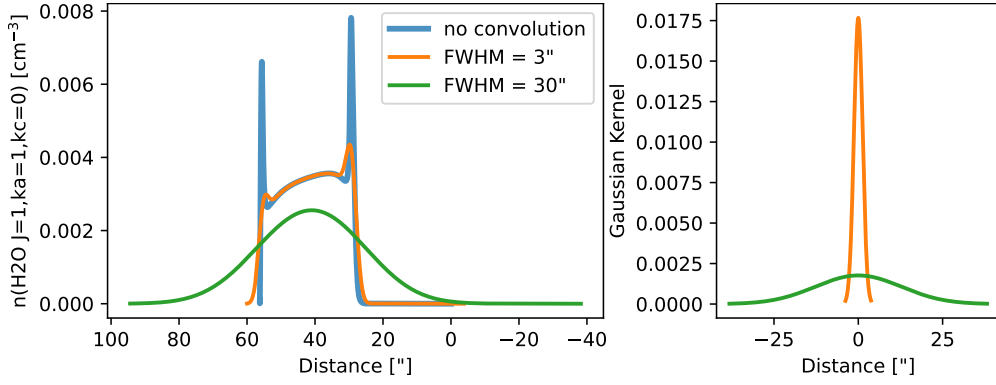


Figure 16: Illustration of the Convolution Process. The left panel shows the original line profile (blue) alongside the profiles convolved with Gaussian PSFs of resolutions 3'' (orange) and 30'' (green). The right panel shows the corresponding Gaussian PSFs, normalized and truncated at  $3\sigma$ .

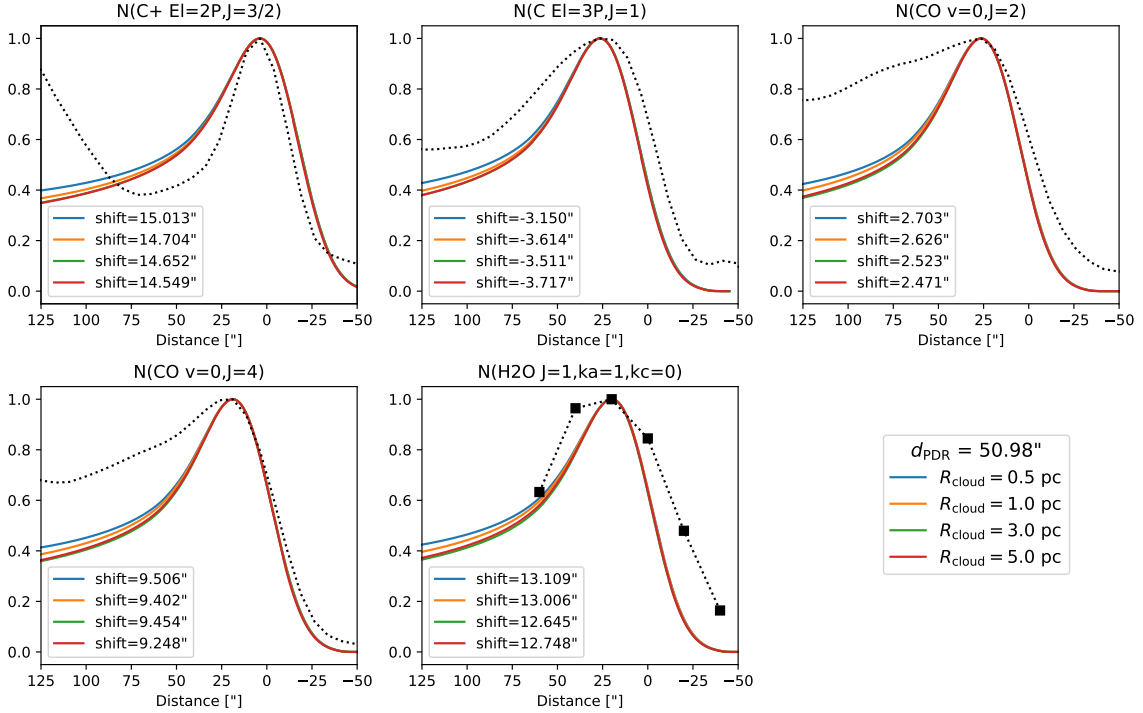


Figure 17: Comparison of normalized line profiles for different cloud radii:  $R_{\text{cloud}} = 0.5 \text{ pc}$  (blue),  $1.0 \text{ pc}$  (orange),  $3.0 \text{ pc}$  (green), and  $5.0 \text{ pc}$  (red). The profiles are shifted to align with the peak locations in the observational data (dotted lines), with the corresponding shifts for each model indicated in the legend.